Nanoscale

Layer-controlled synthesis of WO₃ ordered nanoporous films for optimum electrochromic application

Hongwen Zhang, Guotao Duan,* Guangqiang Liu, Yue Li, Xiaoxia Xu, Zhengfei Dai, Jingjing Wang and Weiping Cai*

We report on a layer-controlled fabrication of two-dimensional (2D) WO₃ ordered nanoporous films via a step-by-step template-assisted strategy. For this purpose, a polystyrene sphere monolayer colloidal crystal (MCC), capable of intact transfer, is adopted as the fabrication template. WO₃ nanoporous films with a monolayer (L1), bilayer (L2) and trilayer (L3) were typically constructed and technical analysis illustrates that each layer is composed of fully crystalline monoclinic WO₃ nanoparticles and aggregated skeletons possessing hexagonally ordered arrangements at long range. Electrochromic characterization reveals that the ITO-based WO₃ nanoporous films have long cycling stability over time and improved cation insertion/extraction capacities with increasing film layer. The inserted/extracted cations of the L2 film are nearly twice that of L1, while slightly inferior to that of L3. For the L3 film, the excessive layer thickness results in longer cation diffusion path lengths, leading to relatively poor charge reversibility. Therefore, the WO₃ nanoporous bilayer films prepared in our work show optimum electrochromic properties after comprehensive characterization. Additionally, the uniform nanoporous film prepared by the proposed strategy can be successfully constructed onto a curved ceramic substrate with rough surfaces, which is still a challenge for traditional spin- or dip-coating methods. This substrate-compatible feature will facilitate construction of specific functional devices and layer-controlled fabrication by a low-cost strategy could find promising applications in chemical sensors, electrochromic windows, and so on.

Introduction

Tungsten oxide (WO₃) is an indirect bandgap semiconductor with outstanding optical and electrical behavior[1] that makes it a promising candidate in applications of catalysts,[2–5] smart windows,[6–8] and chemical sensors.[9–11] In particular, WO₃ films composed of nanoarchitectures with diverse sizes and morphologies have attracted substantial attention in exploring gas sensing devices and electrochromic electrodes.[12–16] Much research on the formation of WO₃ thin coatings was focused on the one step direct-obtainment routes, such as vacuum evaporation, laser ablation, and sputtering methods, through which WO₃ nanomaterials were directly deposited on appropriate substrates to form desired film.[12,16–18] Alternatively, precursor preparation and subsequent spin- or dip-coating operation could be a widely applied approach for the construction of WO₃ thin films.[19–21] However, these two mentioned techniques usually show some obvious drawbacks. For instance, direct-obtained methods usually have the acknowledged disadvantages of high cost, high temperature or high vacuum

dependence, and complicated operation, while WO₃ thin films obtained by coating-assisted techniques are mostly limited to flat substrates, difficult to maintain uniform on a large scale, and usually exist in irregular interstitial areas and inhomogeneous aggregations, resulting in poor repeatability and uncertain performance of the finally obtained WO₃ films. Lately, some template-mediated methodologies,[22–26] involving precursor solutions, have been investigated intensively and proven very successful for introducing pores with sizes ranging from several nanometers to tens of microns, leading to an improvement in the inner surface area of the nanomaterials.[27,28] For this method, aside from its straightforward character and low cost, template-induced limitation domains can ensure localization of the precursor solutions to some extent, leading to fabrication of films with good homogeneity.[29] Commonly, nanoporous structured films are obtained by post-removal templates such as block-copolymers,[29,30] polymethylmethacrylate (PMMA) spheres,[28] colloidal silica crystals,[31] and so on. In particular, polystyrene spheres (PSs) are utilized quite intensively in nanoporous material preparations because of the facility for introducing nanopores,[27,28] tailorability in template patterns,[32–35] diversity in post-removal methods,[36–38] and simplicity in operations. The vertical drying method is conventionally utilized for the fabrication of three-dimensional PS crystal templates.[39,40]

Key Lab of Materials Physics, Anhui Key Lab of Nanomaterials and Nanotechnology, Institute of Solid State Physics, Chinese Academy of Sciences, Hefei, 230031, Anhui, P. R. China. E-mail: duangt@issp.ac.cn; wpcai@issp.ac.cn1

After infiltration of the precursors and subsequent removal of the templates, inverse opal films are obtained. However, the fabrication of large-area, highly ordered and crack-free inverse opals by conventional methods is still a challenge. B. Hatton et al.[41] proposed an improved "coassembly" method, which not only overcame the mentioned drawbacks of the traditional methods to some extent but also illustrated the ability to further modulate the nanostructure and chemical composition of the inverse opals. For example, multilayers with different pore sizes can be fabricated by successive layer deposition. Also, hetero-structured inverse opals can be obtained by changing the precursors for each deposition. However, each deposition process will induce not a single layer, but several layers, which are composed of PSs with the same size. In addition, the reactive transformation routes for the heterojunctions are quite limited. Therefore, methods allowing precise tailoring of a single layer of inverse opal films are rarely reported.

A gas–liquid–solid interface self-assembled PS monolayer colloidal crystal (MCC) with a large area can be disengaged integrally from its initial substrate when immersed into water, by floating on the water surface, and subsequent transfer onto the desired substrate.[42] The transfer process can even be performed with an insulting substrate or a curved surface. What's more, the transfer feature provides the possibility for individual control of each layer by alternate operation between transferring PS MCC and penetrating precursors, which further realizes precise modulation of the structure, morphology, chemical composition (doping, hetero-structured films, and so on), the thickness of the obtained films, and finally their properties and performances.

In present work, we will report layer-controlled generation of WO_3 ordered nanoporous films via step-by-step precursor-penetration on transferred PS MCC templates. The proposed synthetic procedure for porous films is focused on "single-layer-control" and appears to be the most promising candidate for the utmost modulation of the thickness, nanostructure and chemical composition of films. We also evaluated the electro-chromic properties of the obtained films, aiming at thickness-related optimum smart window applications. The films prepared by the proposed strategy also had the advantages of low cost, large area, substrate compatibility and good uniformity. The porosity characteristics, together with these features, would offer potential superiority in practical functional device fabrications of WO_3-based electrochromism and chemical sensing.

Experimental

Materials

All the chemical reagents were analytically pure and used as-received without further purification. The suspensions of PSs (500 nm in diameter, 2.5 wt% dispersion in water) were purchased from Alfa Aesar Corporation. Glass slides, which were taken as the initial substrates for PS MCC self-assembly, were commercially achieved and pre-cleaned according to reported procedures.[43] Indium-tin oxide (ITO) coated glasses (2 × 2 cm²) with a sheet resistance of 50 Ω sq⁻¹ were used as conductive substrates. Water (18.2 MΩ cm) was obtained from an ultrafilter system (Milli-Q, Millipore, Marlborough, MA).

Precursor solution

Firstly, 0.125 g tungstic acid powder was dispersed into a 5 ml hydrogen peroxide solution (30 wt%, Aladdin). Secondly, the obtained suspension liquid was heated to 80 °C and kept for 30 min with a magnetic rotor stirred continuously, forming the colorless colloidal precursor solutions (0.1 M). Thirdly, 2 drops of 0.5 M Triton X-100 solutions were added into the precursor to improve its hydrophilicity.

PS MCC on glass slides

The initially used large area (25 mm × 50 mm) PS MCC was synthesized by gas–liquid–solid interface self-assembly method, as described elsewhere.[44,45] In short, the suspension of mono-dispersed PSs were mixed with ethanol at a ratio of 1 : 1 and ultrasonically treated for 30 min. The pre-cleaned glass slide was taken as the substrate and about 3 ml deionized water was dropped above it. Then, 50 μl mixed PSs suspension was pipetted and carefully dropped onto the surface of the deionized water. When it reached equilibrium state, close-packed ordered PS MCC was self-synthesized on the surface of deionized water. After complete evaporation of deionized water naturally, the glass slide based PS MCC was readily achieved. The as-obtained MCC template could be integrally removed when immersed into water and be picked up by other substrates.

PS MCC transferred onto ITO substrates

The freshly fabricated PS MCC on glass slides possesses the feature of transferability. The transfer process from the glass slide to a new surface is illustrated in Fig. 1 (a–d). When immersed into water, the PS MCC template was separated from the glass slide and integrally floated on the surface of the water. Then, an ITO substrate was used to pick up the template carefully. After drying naturally, the as-transferred PS MCC template, together with the new substrates, were treated at 110 °C for 20 minutes to form a firm contact with each other.

WO_3 ordered nanoporous film with controlled layers

The transferred PS MCC on the new substrate was firstly surface-modified by irradiation in an ultraviolet ozone cleaner for 5 minutes to improve its mechanical flexibility and surface hydrophilicity. Then, 4 μl tungstic acid precursor solutions were slowly dropped onto the fixed PS MCC on a ITO substrate with a quantitative pipette (Fig. 1e). Because of the template-induced limitation domain the dropped precursors, with good hydro-philicity, quickly penetrated into the spaces between the surface modified PS MCC templates and the substrate. A thin tungstic acid film together with ordered PS arrays was formed after drying at 60 °C for 1 hour (Fig. 1f). Finally, PSs were removed upon calcination in an oven at 450 °C for 2 hours, inducing a 2D WO_3 ordered nanoporous monolayer (Fig. 1g). For the formation of bi-layer WO_3 nanoporous film, the previous bare ITO
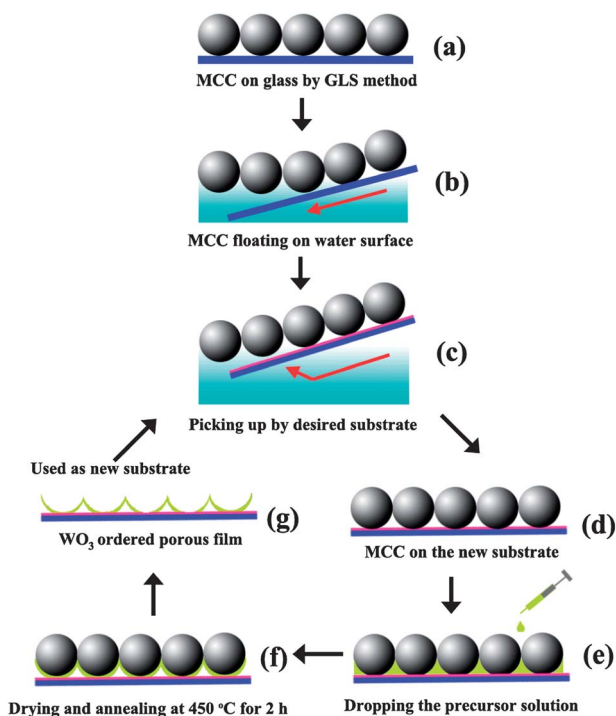
Fig. 1 Schematic illustration of step-by-step template-assisted route for fabrication of 2D WO_3 ordered nanoporous films with controlled layers.

substrate used in PS MCC transferring process was replaced by the freshly prepared WO_3 ordered nanoporous monolayer (Fig. 1c), while subsequent treatments were simply repeated as mentioned above. Due to this synthesis strategy, film with tri-layers were also readily obtained. In brief, a layer-controlled 2D WO_3 ordered nanoporous film can be synthesized *via* a step-by-step template-assisted route.

Technical characterization

The morphologies of the as-obtained films were observed by a field emission scanning electron microscopy (FE-SEM, FEI Sirion 200). The crystal structure was analyzed using an X-ray diffractometer (XRD, the Philips X'Pert) with copper Kα radiation ($\lambda = 0.15406$ nm) at room temperature. The Raman scattering spectra of the films before and after calcination were recorded with a macroscopic confocal Raman spectrometer (LABRAM-HR, France). Transmission electron microscopy (TEM), high-resolution transmission electron microscopy (HR-TEM), and selected area electron diffraction (SAED) studies were performed on a JEM-200CX operated at 200 kV. The optical absorption spectra for nanoporous films at the bleached and colored states were recorded *via* a Cary-5E UV-vis-NIR spectrophotometer.

Electrochromic measurements

Electrochromic behaviors of the obtained 2D WO_3 ordered nanoporous films with diverse layers were studied on a conventional three-electrode electrochemical workstation (CIH660c, Shanghai Chenhua Instruments, Inc.). The

electrochemical test cell was filled with an electrolyte of 1.0 M $LiClO_4$ in propylene carbonate (PC). Before electrochemical tests, the electrolyte was bubbled with nitrogen for several hours to reduce its content of oxygen. The layered WO_3 ordered nanoporous films on the ITO substrate were vertically immersed into the electrolyte and acted as the working electrodes. A platinum foil and Ag/AgCl electrode were taken as the counter and reference electrodes, respectively.

Results and discussion

PS MCC templates

Order-arranged PS MCC with large area can be fabricated *via* a gas–liquid–solid interface self-assembly method, as mentioned in the Experimental section. The initial synthesis of PS MCC is conduced typically on glass slides for two reasons. Firstly, the formation of large area and high quality PS MCC requires smooth, ultra-clean and super-hydrophilic surfaces. For this purpose, the substrates should be correctly chosen and rinsed according to the procedures reported by Haynes *et al.*,[43] in which strong acid is used to remove organic impurities. However, the surface of conducting glasses is commonly not smooth enough and conducting layers might be destroyed during the rinsing process. Secondly, if taking conducting glass as initial substrate, the PS MCC will contact strongly with the conducting layer and will be difficult to separate from the substrate when immersed in water, which means that transfer of PS MCC will not be perfectly performed. Fig. 2a shows a photograph of the as-assembled MCC based on 500 nm PSs. It indicates that the PS MCC on the glass substrate has an area of up to 25 mm × 50 mm, and when tilted, the MCC template mostly shows a blue color, revealing its order and uniform arrangements.[38] When transferred to the ITO substrate, the FE-SEM observation (Fig. 2b) shows that the PSs are hexagonally close-packed with each other, forming a 2D colloidal crystal with long range order.

This transfer of PS MCC possesses distinct advantages for the synthesis of porous materials. For example, by simple layer-by-layer stacking of transferred PS MCC, 3D PS colloidal crystals with precisely controlled thickness can be obtained, which can be used as pristine templates for formation of inverse opal metal oxides with special electrical and optical properties.[42] Secondly, hetero-junction porous functional multilayers, with tuned surface energies and improved mechanical
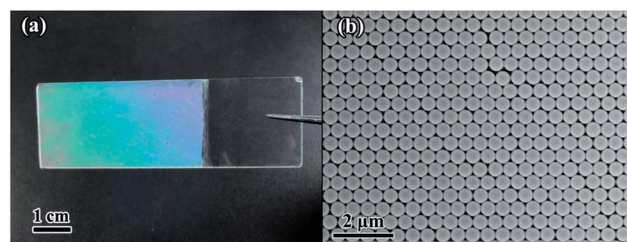
Fig. 2 (a) Photograph of as-assembled PS MCC on a glass slide *via* the gas–liquid–solid interface self-assembly method. (b) FE-SEM images of the PS MCC transferred onto flat ITO substrate.

properties,[43,44] can be readily prepared *via* independent construction of each layer. For simplicity, we will demonstrate the typical fabrication of homogeneous WO_3 nanoporous monolayer (L1), bilayer (L2) and trilayer (L3) films in the present work.

Monolayer WO_3 ordered nanoporous film

Fig. 3 shows typical XRD investigation of films before and after removal of PS MCC by annealing at 450 °C for 2 hours, respectively. According to the sharp reflections, both two films possess good crystallinity. This also indicates that the pristine film, directly derived from drying the precursors at 60 °C for 1 hour, has a crystalline structure of peroxopolytungstic acid ($[WO_2 \cdot (O_2) \cdot H_2O] \cdot 1.66H_2O$, JCPDS no. 050-0234). Upon increasing the temperature, a dehydration process occurs, finally leading to the formation of anhydrous tungsten oxide. The peaks identified in Fig. 3b can be ascribed to the monoclinic WO_3 structures (JCPDS no. 075-2072) with lattice parameters of $a = 7.274$ Å, $b = 7.501$ Å, $c = 3.824$ Å and a space group of $P2/a$. Both the monoclinic phase and corresponding dehydration process have been similarly reported in other works.[45]

Raman spectroscopy was also employed to evaluate the degree of dehydration upon calcination, as demonstrated in Fig. 4. The peaks between 600 and 900 cm^{-1} could be attributed to the bending modes of W–O,[23] while those around 583, 914 and 980 cm^{-1} in pristine films were readily assigned to vibrations of peroxo groups in $W(O_2)$,[46] which disappeared after annealing. At the same time, obvious intensity enhancements were found in the annealed film for peaks situated at 708 and 804.2 cm^{-1}, together with which the 270 and 322 cm^{-1} modes were the four strongest of monoclinic WO_3.[20] The bridging (O–W–O) vibrations, namely the *ca.* 640 cm^{-1} band, show good sensitivity to hydration and can be used as flags to illustrate the hydration level of WO_3.[47] For pristine samples, it showed a well defined peak at 640 cm^{-1}. However, the peak disappeared upon calcination, leaving a tiny shoulder for the enhanced band of
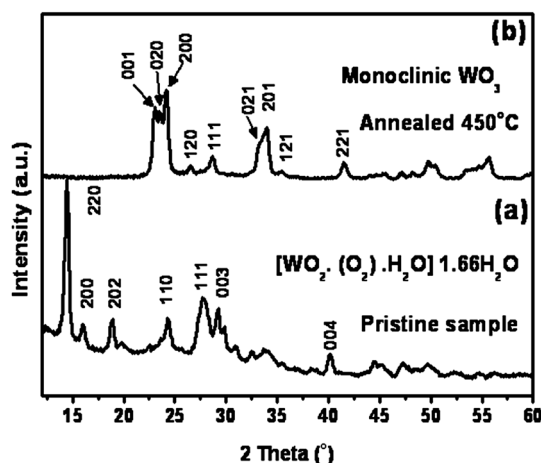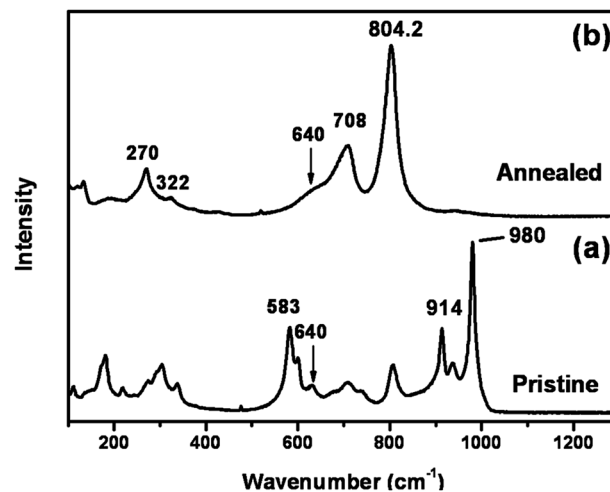

Fig. 4 Raman spectra for a pristine film obtained by drying precursors at 60 °C (a) and a nanoporous film upon calcination at 450 °C for 2 hours (b).

708 cm^{-1}. The peak changes indicated a successful transformation from peroxo compounds to monoclinic tungsten oxide.

Fig. 5a typically shows a low magnification FE-SEM image of the as-prepared L1 film. Because of sufficient pretreatment to the PS MCC on an ITO substrate prior to infiltration of the precursors, the hexagonally ordered PS templates formed a firm contact with the substrate and surfaces, which showed superhydrophilic properties. After removal of PS MCC, a perfect template replica appeared and large-area (*ca.* 4 cm^{-2} in present work) ordered porous films with limited cracks, domain boundaries, and other defects were finally obtained. A two-dimensional Fourier transform of the 10 × 10 μm^2 region of the porous array was performed with image processing software, as illustrated in the inset of Fig. 5a. The observed
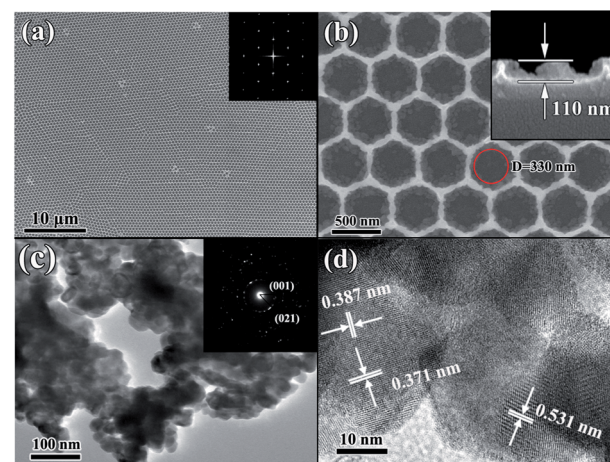

Fig. 5 Typical FE-SEM images (a and b) and TEM observations (c and d) of monolayer WO_3 ordered nanoporous films, prepared by taking transferred PS MCC as the template and by post-removal of PSs. Inset in (a): Fourier transform of the low magnification image of a 10 × 10 μm^2 region. Inset in (b): fracture cross-section FE-SEM observation for monolayer film. Inset in (c): corresponding SAED pattern of skeletons in porous film, indicating its polycrystalline nature.


Fig. 3 XRD patterns of films prepared before (a) and after (b) removal of PS MCC templates by annealing at 450 °C for 2 hours.

clear and uniform spots confirm that the typically observed WO$_3$ nanoporous monolayer has long-range order. In addition, the hexagonal pattern indicates that the nanoporous film exhibits a hexagonally ordered arrangement, revealing a perfect template-replica process.[29] Fig. 5b shows a further magnified FE-SEM image, which readily demonstrates ordered quasi-hexagon skeleton arrays with a space between the neighboring ones of 500 nm and a thickness of ca. 110 nm (inset of Fig. 5b). The skeletons have tough irregular surfaces and are apparently composed of aggregated nanoparticles. Dark and smooth circles with diameters of ca. 330 nm in the center of each isolated quasi-hexagon skeleton are observed as ITO substrates (marked in Fig. 5b), which were induced by surface contact between the PSs and ITO substrate during heating process.

Fig. 5c and d shows the TEM image, SAED pattern and HR-TEM observation of WO$_3$ skeletons scraped from the as-obtained ordered nanoporous film on the ITO substrate. They show that the skeletons of the WO$_3$ nanoporous films are composed of aggregated nanoparticles with an average grain size of ca. 30 nm. The distorted void among those nanoparticles (Fig. 5c) probably originates from the nanopores of the porous film produced by removal of PS templates. The corresponding SAED pattern (inset of Fig. 5c) of the skeletons shows that the nanoporous film is polycrystalline and the main two inner diffraction rings can be readily assigned to the (001) and (021) crystal planes of the monoclinic WO$_3$ phase (JCPDS no. 075-2072), respectively. Fig. 5d shows a HR-TEM image of several isolated nanoparticles, which demonstrates clear 2D ordered lattice fringes, indicating that the nanoparticles are well crystallised. Furthermore, the measured interplanar distance values of 0.387 and 0.371 nm for one nanoparticle are in good agreement with the (001) and (020) planes of the monoclinic WO$_3$ phase, respectively. The lattice fringe d-spacing of 0.531 nm, calculated from another isolated particle, can be indexed to the (110) plane. The TEM observation agrees well with results of XRD measurement.

On the basis of above analysis, we conclude that the WO$_3$ monolayer with an hexagonally arranged porous structure and an almost defect-free character can be achieved after subsequent removal of the transferred PS MCC template upon calcination. The skeletons of the monolayer are polycrystalline and composed of well-crystallized monoclinic WO$_3$ nanoparticles with an average size of 30 nm.

Multi-layered WO$_3$ ordered nanoporous film

Fig. 6 shows FE-SEM images of WO$_3$ ordered nanoporous bi- and tri-layer films prepared via transferring PS MCC and penetrating precursors in turn, as described in the Experimental section. Fig. 6a and c are low magnification FE-SEM images of the as-prepared WO$_3$ L2 and L3 film, respectively. It's apparent that both two films show flat and ordered porous surface nanostructures, and the films in the observation range are uniform and isotropic to a certain extent, except for some limited surface cracks probably due to increased surface roughness of the substrate in the transferring PS MCC process.
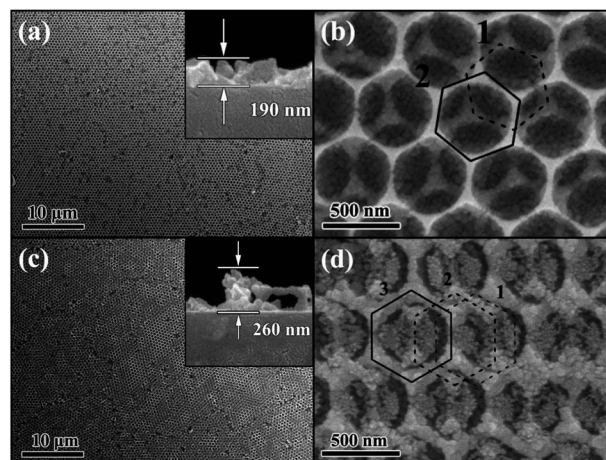
Fig. 6 Typical FE-SEM images of bi- (a and b) and tri-layer (c and d) WO$_3$ ordered nanoporous films on flat ITO substrates prepared by repeated operations of transferring 500 nm based PS MCC, penetrating precursors, and calcination. Insets in (a) and (c) are fracture cross-section observations for bi- and tri-layer films, respectively.

The fracture cross-section FE-SEM observations illustrate that the thicknesses are 190 and 260 nm for L2 and L3 films, respectively. Fig. 6b is a typical FE-SEM image of the L2 WO$_3$ nanoporous film with a higher magnification, in which two overlapped layers of the nanoporous film (labeled with Arabic numerals of 1 and 2, respectively) can be observed readily. What's more, both the skeletons in the bottom and upper layers retain their hexagonally ordered arrangements. For L3 (Fig. 6d), the top layer (marked as 3) clearly shows quasi-hexagonal skeleton ordered arrays in the observation range and each quasi-hexagon is filled with nanoparticle aggregates. After careful analysis, the aggregations can be divided into two types, which originate from contributions of the first and second layers. A slight collapse of the skeletons was found for the bottom two layers, probably due to the repeated annealing treatment. However, the ordered arrangement of the skeleton arrays can still be readily distinguished, in which the hexagonal repeating units are labeled by Arabic numerals of 1 and 2 in Fig. 6d, respectively. Also, circles appearing as ITO substrate in the monolayer are not observed both for L2 and L3 films. The disappearance of these circular voids should be ascribed to spatial occupation of the latter layers and collapse of the skeletons.

In brief, the nanoporous WO$_3$ bi- and tri-layers with hexagonally ordered arrangements can be obtained via repeated operations of transferring the PS MCC templates and penetrating the precursors. It's reasonable to conclude that similar WO$_3$ nanoporous films with more layers can be prepared by the proposed strategy. In present work, we showed typical step-by-step multilayer construction of porous films with the same pore sizes and homogenous materials of WO$_3$ for each layer. However, by simply changing the PS MCC templates or precursors for each layer, it's reasonable that hetero-apertured or hetero-junction multilayers can be readily obtained through this proposed strategy.[48-52]

Electrochromic properties of WO₃ nanoporous films

Electrochromic behaviors of ITO-based 2D WO$_3$ ordered nanoporous films were evaluated on the test cell of a traditional three-electrode electrochemical workstation. A cyclic voltammogram (CV) of a monolayer WO$_3$ ordered nanoporous film (Fig. 7a), performed between −0.6 V and 1.0 V with a sweep rate of 50 mV s^{-1} at room temperature, showed a typical curve shape and well-defined anodic peak, which was quite similar to prior reports on WO$_3$ electrochromic films.[53–55] Slightly shrinking the peak current density during 100 successive cycles indicates that the WO$_3$ ordered nanoporous monolayer possesses good electrochemical cycling stability, which arises from the good crystallization of the WO$_3$ nanoparticles in the skeletons of the WO$_3$ nanoporous film. For comparison, CV for L2 and L3 were also shown in Fig. 7b, in which the outline of all recorded voltammograms were similar to each other, although the peak current densities showed a significant increase for L2 and L3 films. The increase of the peak current densities in multiple layers reveals that more trap sites for cation insertion/extraction were supplied during the electrochemical process. This can be explained by differences in the amounts of nanoparticles that actually induced electrochromism. As demonstrated in FE-SEM observations, the second and/or third layer for L2 and L3 nanoporous films would occupy the voids produced by previous nanoporous layers, which means that on immersion into the electrolyte, more crystallized WO$_3$ nanoparticles will contact with the electrolyte and act as trap sites when biased.

Curves for the repetitive chronoamperometry tests of the WO$_3$ nanoporous films, performed by applying successive voltage steps of −0.6 V and 1.0 V for 60 s, respectively, are shown in Fig. 8a, in which the almost-unchanged intensities and curve shapes for each film confirm that all porous films have good electrochemical stability during the repetitive cation insertion/extraction processes. All the films show a rapid decline in current after the polarity was immediately switched and biased for 60 s. However, the current of L1 decays sharply relatively to that of the L2 and L3 films, indicating that more layers in the electrochromic porous films will suppress cation insertion and extraction effectively (Fig. 8a and b). Also, the insertion and extraction capacities for porous films can be evaluated by comparing integrals of the potentiostatic curves over positive and negative bias intervals respectively, as shown in Fig. 8c. This clearly shows that the charge densities of L3 are slightly larger than that of L2, but twice that of L1. The insertion/extraction reversibility (Fig. 8d) for L1 and L2 are similar, and both reached values of larger than 90%. But when one more layer is stacked (L3), the reversibility decreased distinctly down to *ca.* 86%. Fig. 9 shows the transmittance spectrum of film samples at the bleached and colored states (biased at 1.0 V and −0.6 V for 60 s, respectively). This reveals a tendency towards a decline in transmittance for both the bleached and colored states with increasing film layer. When the nanoporous films were biased at −0.6 V, both electrons and lithium ions were injected into cation trap sites and the corresponding transmittance spectra decreased considerably within the spectra of 550–1200 nm, resulting in an obvious optical contrast (typically the L3 film, inset of Fig. 9).

As a result, the WO$_3$ ordered nanoporous films with diverse layers, as electrochromic electrodes have long cycling stability. We also concluded that the cation insertion/extraction capacities were improved by increasing the film layer, owing to more trap sites in contact with surrounding electrolyte. Compared to that of L1, however, an obvious advantage was observed for L2, which was slightly inferior to L3. For L3, the relatively lower cation insertion/extraction efficiency and poorer reversibility can be ascribed to the excessive layer thickness, which supplies deeper trap sites and causes a longer cation diffusion path length.

## WO₃ ordered nanoporous films on rough and curved surfaces

Besides most the commonly used flat substrates, curved or even rough surfaces must be utilized without alternative for the construction for some specific functional devices, such as traditional semiconductor gas sensors,[56] surface-enhanced Raman scattering (SERS) devices,[57] and so on. For these substrates, it's quite a challenge to construct a uniform and isotropic nanomaterial layer onto the extreme surface through traditional spinning or dip-coating of the precursors. In our
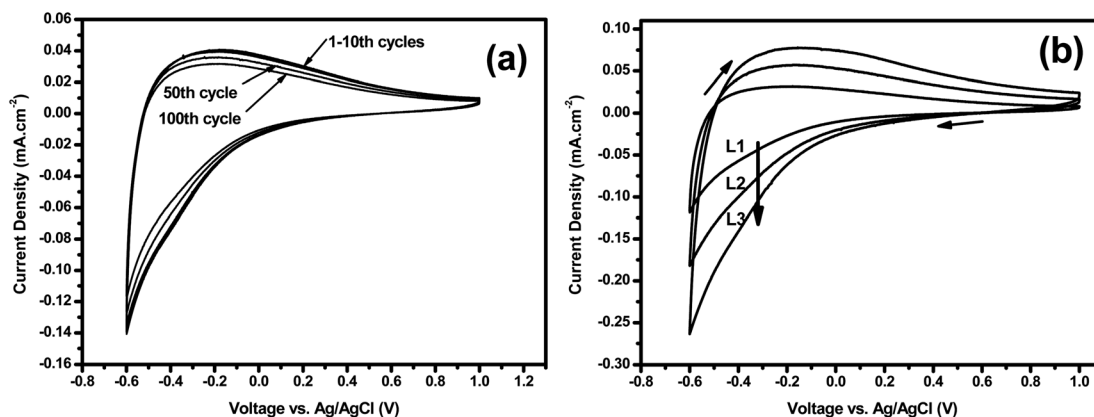
Fig. 7 Cyclic voltammograms (CV) of WO$_3$ ordered nanoporous films obtained in 1.0 M LiClO$_4$ in propylene carbonate at a scan rate of 50 mV s^{-1}. (a) 100 times-repeated CV of the monolayer porous film. (b) Comparison of CV for the porous monolayer (L1), bilayer (L2) and trilayer (L3), respectively.
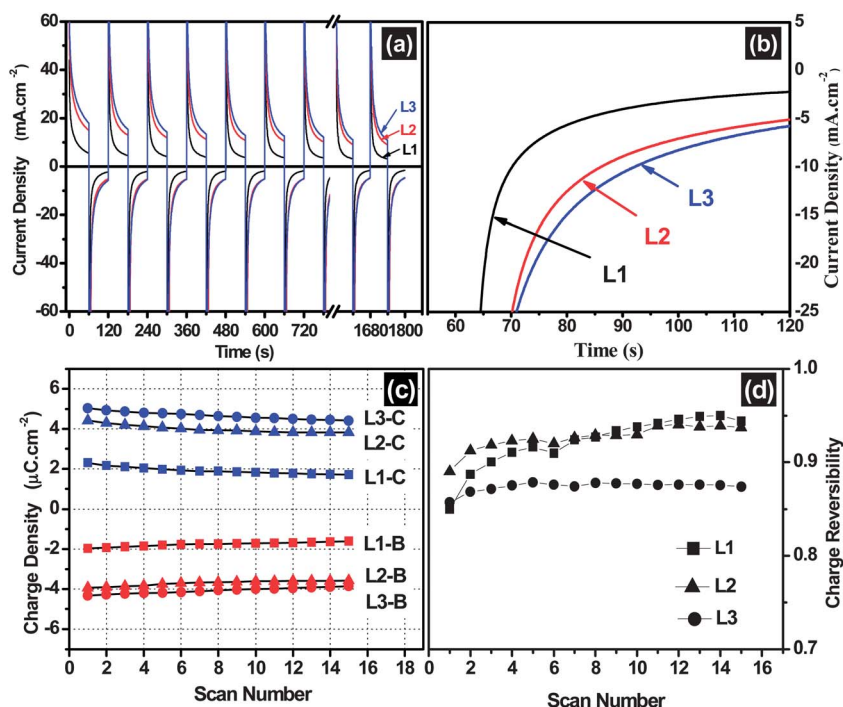
Fig. 8 Electrochemical characterizations during repetitive chronoamperometry (CA) test of WO_3 nanoporous films with diverse layers (voltage steps 1.0 V and −0.6 V, step duration 60 s). (a) CA curves of L1, L2 and L3 films for successive cation insertion/extraction steps. (b) A typical cation extraction process with enlarged illustrations. (c) Amount of charge inserted and extracted when the films were positive (colored) and negative (bleached) biased for 60 s. (d) Corresponding charge reversibility values.
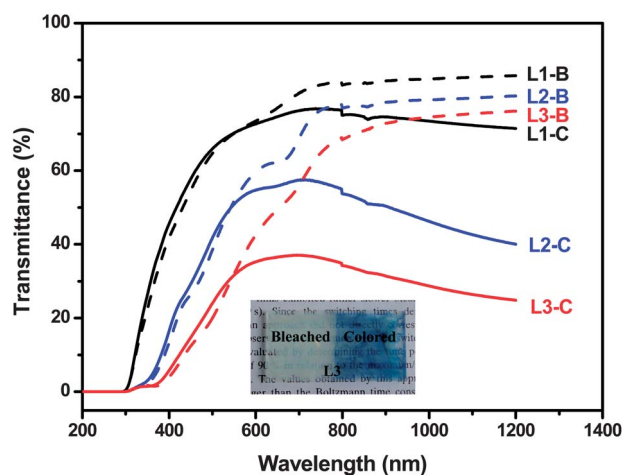
Fig. 9 Transmittance spectra of WO_3 ordered nanoporous films with diverse layers recorded at colored (biased at −0.6 V) and bleached states (biased at 1.0 V). Inset shows typical photographs of the L3 film at those two states, illustrating a distinct optical contrast.

work, the synthesis strategy of template transfer and subsequent precursor penetration was also evaluated for preparation of WO_3 nanoporous films upon extreme substrates. Herein, we take a curved ceramic tube as an example, which has a curvature of 1000 m^{-1} and a rough surface. The inset of Fig. 10a shows macroscopic observation of the curved ceramic tube covered by transferred PS MCC. The corresponding low magnified FE-SEM image clearly depicts that the ordered PS MCC on a large scale

can be successfully transferred onto the curved surface, and shows some wrinkles due to the fluctuation of the substrate surface. However, the hexagonally ordered arrangements were still retained (Fig. 10b). After removal of the templates upon calcination, a template-replica phenomenon was observed again, leaving large area WO_3 nanopores with an ordered arrangement (Fig. 10c and d). This should also be ascribed to the transferability feature of PS MCC, which enables deposition
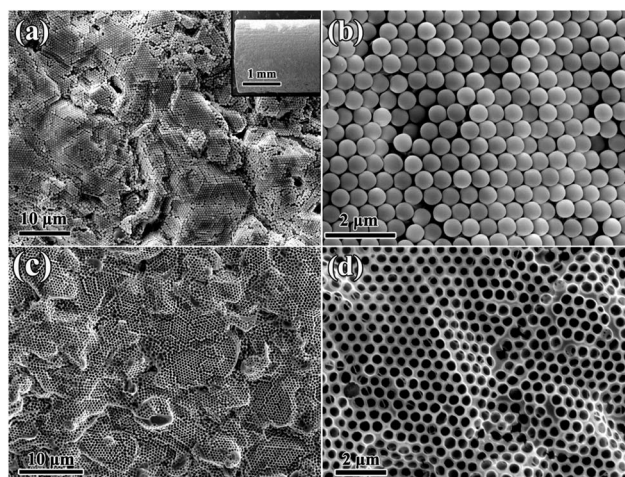
Fig. 10 (a and b) FE-SEM images of transferred PS MCC onto curved ceramic tube with rough surfaces. (c and d) Corresponding WO_3 ordered nanoporous films after removal of PSs upon calcinations.

of ordered PS templates onto desired substrates and firm contact with each other.

Conclusions

In summary, a polycrystalline WO_3 nanoporous monolayer, with features of large area and good uniformity, being defect-free and possessing an hexagonally ordered arrangement, was readily prepared on ITO substrates by taking transferred PS MCC as a template. With the transfer of PS MCC, penetrating precursors, and subsequent calcination in turn, such WO_3 ordered nanoporous films with precisely controlled layers were successfully fabricated. Each layer in the WO_3 multilayer films almost retained its hexagonal arrangement and the film as a whole demonstrated ordered nanoporous features. Electro-chromic tests illustrate that the nanoporous films had good cycling stability and, compared with WO_3 L1 and L3 films, the L2 ones show optimum electrochromic properties with respect to comprehensive characterization of the insertion/extraction capacities, cation diffusion efficiency, and charge reversibility. Besides this, the nanoporous film made by the proposed strategy can be successfully constructed onto a curved ceramic substrate with a rough surface. These layer-controlled WO_3 nanoporous films on desired substrates prepared by a low-cost strategy will find promising applications in chemical sensors, electrochromic windows, and so on.

Acknowledgements

Notes and references

1 H. D. Zheng, J. Z. Ou, M. S. Strano, R. B. Kaner, A. Mitchell and K. Kalantar-Zadeh, *Adv. Funct. Mater.*, 2011, **21**, 2175–2196.

2 Z. G. Zhao and M. Miyauchi, *Angew. Chem., Int. Ed.*, 2008, **47**, 7051–7055.

3 W. Lee, D. Kim, K. Lee, P. Roy and P. Schmuki, *Electrochim. Acta*, 2010, **56**, 828–833.

4 B. Cole, B. Marsen, E. Miller, Y. F. Yan, B. To, K. Jones and M. Al-Jassim, *J. Phys. Chem. C*, 2008, **112**, 5213–5220.

5 R. Solarska, R. Jurczakowski and J. Augustynski, *Nanoscale*, 2012, **4**, 1553–1556.

6 S. H. Baeck, K. S. Choi, T. F. Jaramillo, G. D. Stucky and E. W. McFarland, *Adv. Mater.*, 2003, **15**, 1269–1273.

7 G. A. Niklasson and C. G. Granqvist, *J. Mater. Chem.*, 2007, **17**, 127–156.

8 J. Z. Ou, S. Balendhran, M. R. Field, D. G. McCulloch, A. S. Zoolfakar, R. A. Rani, S. Zhuiykov, A. P. O'Mullane and K. Kalantar-zadeh, *Nanoscale*, 2012, **4**, 5980–5988.

9 M. Penza, C. Martucci and G. Cassano, *Sens. Actuators, B*, 1998, **50**, 52–59.

10 J. Polleux, A. Gurlo, N. Barsan, U. Weimar, M. Antonietti and M. Niederberger, *Angew. Chem., Int. Ed.*, 2006, **45**, 261–265.

11 M. D'Arienzo, L. Armelao, C. M. Mari, S. Polizzi, R. Ruffo, R. Scotti and F. Morazzoni, *J. Am. Chem. Soc.*, 2011, **133**, 5296–5304.

12 V. Khatko, S. Vallejos, J. Calderer, E. Llobet, X. Vilanova and X. Correig, *Sens. Actuators, B*, 2007, **126**, 400–405.

13 B. Deb, S. Desai, G. U. Sumanasekera and M. K. Sunkara, *Nanotechnology*, 2007, **18**, 285501, DOI: 10.1088/0957-4484/18/28/285501.

14 G. Z. Xie, J. S. Yu, X. Chen and Y. D. Jiang, *Sens. Actuators, B*, 2007, **123**, 909–914.

15 E. Rossinyol, A. Prim, E. Pellicer, J. Arbiol, F. Hernandez-Ramirez, F. Peiro, A. Cornet, J. R. Morante, L. A. Solovyov, B. Z. Tian, T. Bo and D. Y. Zhao, *Adv. Funct. Mater.*, 2007, **17**, 1801–1806.

16 Y. Shen, T. Yamazaki, Z. Liu, D. Meng, T. Kikuta and N. Nakatani, *Thin Solid Films*, 2009, **517**, 2069–2072.

17 G. J. Fang, Z. L. Liu and K. L. Yao, *Int. J. Inorg. Mater.*, 2002, **17**, 139–144.

18 K. J. Lethy, D. Beena, R. V. Kumar, V. P. M. Pillai, V. Ganesan and V. Sathe, *Appl. Surf. Sci.*, 2008, **254**, 2369–2376.

19 K. Kalantar-zadeh, A. Vijayaraghavan, M. H. Ham, H. D. Zheng, M. Breedon and M. S. Strano, *Chem. Mater.*, 2010, **22**, 5660–5666.

20 C. Santato, M. Odziemkowski, M. Ulmann and J. Augustynski, *J. Am. Chem. Soc.*, 2001, **123**, 10639–10649.

21 L. Francioso, M. Russo, A. M. Taurino and P. Siciliano, *Sens. Actuators, B*, 2006, **119**, 159–166.

22 P. Jiang and M. J. McFarland, *J. Am. Chem. Soc.*, 2005, **127**, 3710–3711.

23 M. Breedon, P. Spizzirri, M. Taylor, J. du Plessis, D. McCulloch, J. M. Zhu, L. S. Yu, Z. Hu, C. Rix, W. Wlodarski and K. Kalantar-Zadeh, *Cryst. Growth Des.*, 2010, **10**, 430–439.

24 G. T. Duan, W. P. Cai, Y. Y. Luo, Z. G. Li and Y. Lei, *J. Phys. Chem. B*, 2006, **110**, 15729–15733.

25 Y. Li, W. P. Cai and G. T. Duan, *Chem. Mater.*, 2008, **20**, 615–624.

26 L. C. Jia, W. P. Cai, H. Q. Wang, F. Q. Sun and Y. Li, *ACS Nano*, 2009, **3**, 2697–2705.

27 P. Jiang, *Langmuir*, 2006, **22**, 3955–3958.

28 M. Sadakane, K. Sasaki, H. Kunioku, B. Ohtani, W. Ueda and R. Abe, *Chem. Commun.*, 2008, 6552–6554.

29 T. Brezesinski, D. Fattakhova-Rohlfing, S. Sallard, M. Antonietti and B. M. Smarsly, *Small*, 2006, **2**, 1203–1211.

30 S. Sallard, T. Brezesinski and B. M. Smarsly, *J. Phys. Chem. C*, 2007, **111**, 7200–7206.

31 P. Jiang, J. Cizeron, J. F. Bertone and V. L. Colvin, *J. Am. Chem. Soc.*, 1999, **121**, 7957–7958.

32 Y. Li, W. P. Cai, G. T. Duan, B. Q. Cao, F. Q. Sun and F. Lu, *J. Colloid Interface Sci.*, 2005, **287**, 634–639.

33 G. T. Duan, W. P. Cai, Y. Y. Luo and F. Q. Sun, *Adv. Funct. Mater.*, 2007, **17**, 644–650.

34 Y. Li, W. P. Cai, B. Q. Cao, G. T. Duan, C. C. Li, F. Q. Sun and H. B. Zeng, *J. Mater. Chem.*, 2006, **16**, 609–612.

35 G. T. Duan, W. P. Cai, Y. Y. Luo, F. J. Lv, J. L. Yang and Y. Li, *Langmuir*, 2009, **25**, 2558–2562.

36 Y. Li, E. J. Lee, W. P. Cai, K. Y. Kim and S. O. Cho, *ACS Nano*, 2008, **2**, 1108–1112.

37 S. K. Yang, W. P. Cai, L. C. Kong and Y. Lei, *Adv. Funct. Mater.*, 2010, **20**, 2527–2533.

38 J. M. Torres, C. M. Stafford and B. D. Vogt, *ACS Nano*, 2010, **4**, 5357–5365.

39 M. A. Mclachlan, N. P. Johnson, R. M. Rue, La. De and D. W. McComb, *J. Mater. Chem.*, 2004, **14**, 144–150.

40 L. L. Yang, D. T. Ge, J. P. Zhao, Y. B. Ding, X. P. Kong and Y. Li, *Sol. Energy Mater. Sol. Cells*, 2012, **100**, 251–257.

41 B. Hatton, L. Mishchenko, S. Davis, K. H. Sandhage and J. Aizenberg, *Proc. Natl. Acad. Sci. U. S. A.*, 2010, **107**, 10354–10359.

42 G. T. Duan, W. P. Cai, Y. Li, Z. G. Li, B. Q. Cao and Y. Y. Luo, *J. Phys. Chem. B*, 2006, **110**, 7184–7188.

43 C. L. Haynes and R. P. Van Duyne, *J. Phys. Chem. B*, 2001, **105**, 5599–5611.

44 M. Kondo, K. Shinozaki, L. Bergstrom and N. Mizutani, *Langmuir*, 1995, **11**, 394–397.

45 B. Pecquenard, H. Lecacheux, S. Castro-Garcia and J. Livage, *J. Sol-Gel Sci. Technol.*, 1998, **13**, 923–927.

46 N. Tokuro, T. Sanae, Y. Itaru and K. Tetsuichi, *J. Solid State Chem.*, 1991, **90**, 47–53.

47 M. F. Daniel, B. Desbat, J. C. Lassegues, B. Gerand and M. Figlarz, *J. Solid State Chem.*, 1987, **67**, 235–247.

48 Z. Z. Gu, D. Wang and H. Mohwald, *Soft Matter*, 2007, **3**, 68–70.

49 P. Jiang, J. F. Bertone, K. S. Hwang and V. L. Colvin, *Chem. Mater.*, 1999, **11**, 2132–2140.

50 J. C. Lytle, N. R. Denny, R. T. Turgeon and A. Stein, *Adv. Mater.*, 2007, **19**, 3682–3686.

51 L. Hung-Chang, K. K. Rao, J. Jun-Yuan, H. Yu-Jer, G. Tzung-Fang, J. Yean-Ren and W. Ten-Chin, *Sol. Energy Mater. Sol. Cells*, 2011, **95**, 2976–2980.

52 Y. Sun, S.-C. Chien, H.-L. Yip, K.-S. Chen, Y. Zhang, J. A. Davies, F.-C. Chen, B. Lin and A. K. Y. Jen, *J. Mater. Chem.*, 2012, **22**, 5587–5595.

53 M. Deepa, A. K. Srivastava, K. N. Sood and S. A. Agnihotry, *Nanotechnology*, 2006, **17**, 2625–2630.

54 J. M. Wang, E. Khoo, P. S. Lee and J. Ma, *J. Phys. Chem. C*, 2008, **112**, 14306–14312.

55 Y. Z. Zhang, J. G. Yuan, J. Le, L. X. Song and X. F. Hu, *Sol. Energy Mater. Sol. Cells*, 2009, **93**, 1338–1344.

56 J. Huang, X. Xu, C. Gu, M. Yang, M. Yang and J. Liu, *J. Mater. Chem.*, 2011, **21**, 13283–13289.

57 R. J. C. Brown and M. J. T. Milton, *J. Raman Spectrosc.*, 2008, **39**, 1313–1326.